JSR Publications

Available Online

J. Sci. Res. **18** (3), 547-559 (2026)

JOURNAL OF SCIENTIFIC RESEARCH

www.banglajol.info/index.php/JSR

Comprehensive Characterization of $BiFeO_3$ Perovskite Synthesized by Pechini Method with High Photocatalytic Activity

B. S. Meena[1], K. Kumari[1], A. S. Shekhawat[2], M. Meena[1], U. Chandrawat[1*],

[1]Department of Chemistry, Government College, Kota, Rajasthan, India, 324001

[2]Department of Computer Science and Engineering, Manipal University Jaipur, Jaipur, Rajasthan, India, 3033007

Received 4 January 2026, accepted in final revised form 9 June 2026

Abstract

This research focuses on the synthesis of $BiFeO_3$ perovskite by Pechini method with an objective to investigate its potential in carrying out the photo degradation of the basic dye Malachite green under visible light irradiation. The purity and stability of $BiFeO_3$ material was analyzed by different characterization techniques. The FT-IR spectra with the bands at 450 cm^{-1} and 549.68 cm^{-1} showed metal-oxygen bonding accounting for the creation of a perovskite structure, XRD data showed that pure-phase $BiFeO_3$ crystallized into a rhombohedral structure with a crystallite size of 30.06 nm calculated using Scherer's formula. SEM indicated particles in the nano range of 150 nm – 450 nm. Elemental composition from EDX results was close to theoretical values, thus verifying the high purity of the nanoparticles. Band gap was found to be 1.9 eV from UV-DRS. Based on its crystalline nature and band gap, this material may be utilized as a photocatalyst. An initial dye concentration of 40 mg/L and a catalyst dose of 0.75 g/L at 35 °C were found to produce the most optimal results in studies evaluating the influence of initial concentration of dye and catalyst loading on dye degradation. A pseudo-first-order kinetic Langmuir-Hinshelwood expression was used to describe the dye photodegradation.

Keywords: $BiFeO_3$; Malachite green dye; Pechini method; Perovskites; Photocatalytic degradation.

doi: https://dx.doi.org/10.3329/jsr.v18i3.86586 J. Sci. Res. 1**8** (3), 547-559 (2026)

1. Introduction

Rapid industrialization has caused significant pollution on Earth, especially in water, owing to the outflow of industrial waste water. Water contamination is a serious global issue and is now the biggest cause of disease and death worldwide. Since synthetic dyes can block sunshine and oxygen from dissolving in wastewater, two processes essential to aquatic life, their potential carcinogenicity raises severe concerns about their effects on the environment [1].

A highly soluble and widely used chemical, Malachite green is frequently discharged into aquatic environments from a number of sources and has been demonstrated to be

* *Corresponding author:* chandrawatuttra@gmail.com

carcinogenic, teratogenic, and to impair animal reproduction. In waste water treatment and other associated environmental issues, photocatalytic degradation of dyes and organic contaminants is crucial [2,3].

Previous studies have employed a variety of techniques to eliminate Malachite Green [4]. Recent decades have been devoted to the development of numerous novel perovskite-based structures that can be employed as visible-light active photocatalysts while utilizing the maximum amount of solar energy [5,6]. Given their electromagnetic behaviour, structural stability, magneto-resistive qualities, and ability to sustain cations in many different kinds of oxidation states, perovskite-structured ABO_3 compounds have remarkable chemical and physical features. They are suitable for photocatalysis because of these characteristics, which boost their catalytic activity [7]. No study has reported the photocatalysts degradation of Malachite green using $BiFeO_3$ synthesized by Pechini method as a photo catalyst.

Hence, $BiFeO_3$ was chosen for Malachite Green dye degradation in this investigation because of the exceptional photocatalytic capabilities of Bi-based photocatalysts. $BiFeO_3$ has been prepared using a variety of techniques [8-13]. At lower temperatures, these processes fail to create high-purity materials with acceptable resistivity, and they typically demand for high annealing temperatures [14]. To get over these issues, the Pechini process is used to create $BiFeO_3$, and various characterisation techniques are used to analyse at its structural characteristics. The degradation of Malachite green using the Langmuir-Hinshelwood kinetic model is then used to assess the photocatalytic activity of the synthesized material [15,16].

2. Materials and Methods

2.1. *Materials*

All experiments were carried out with de-ionized ultra-pure water using Ultra-pure water purification system (Elix UV 3 model) throughout the study. Iron nitrate nonahydrate ($Fe(NO_3)_3 \cdot 9H_2O$), Bismuth nitrate ($Bi(NO_3)_3$), Ethylene glycol ($C_2H_6O_2$), Nitric acid (HNO_3) and Citric acid ($C_6H_8O_7$) are purchased from Merck (India). Malachite green is obtained from SDS Fine Chem. (P.) Ltd. (India).

2.2. *Synthesis of $BiFeO_3$ perovskite*

$BiFeO_3$ (bismuth ferrite) nanoparticles were synthesized via the Pechini method, an established sol-gel process that yields extremely pure and uniform complicated oxides. The process began with the preparation of stoichiometric proportions of bismuth nitrate pentahydrate ($Bi(NO_3)_3 \cdot 5H_2O$) and iron nitrate nonahydrate ($Fe(NO_3)_3 \cdot 9H_2O$). Each precursor was dissolved separately in 50 mL deionized H_2O to form 1 M solutions. Since bismuth nitrate is highly prone to hydrolysis, its dissolution was performed using deionized water and HNO_3 to ensure complete solubility and prevent insoluble hydroxide formation.

To allow uniform metal ion distribution and forming a homogeneous solution, the two solutions were mixed and stirred for 30 minutes.

To enhance solution stability and prevent unwanted precipitation, citric acid was added as a chelating agent in molar ratio of 4:1 relative to the total metal ion concentration. Citric acid formed metal-citrate complexes, preventing phase segregation and ensuring molecular-level uniformity. The solution was stirred for another 30 min at room temperature to complete chelation. Subsequently, as a polymerization agent, ethylene glycol was poured in a 40:60 weight ratio (ethylene glycol to citric acid). This facilitated the polymerization process, forming a polymeric resin with evenly distributed metal ions. The mixture was stirred continuously for 2 hours, resulting in a clear, blackish-red sol.

The sol was subjected to controlled heating at 70-75 °C, initiating the polymerization reaction and converting the sol into a viscous green gel. This transformation was accompanied by the evolution of brown fumes, indicating the decomposition of organic components. The gel was dried in an oven at 70 °C to remove residual water and volatile compounds, yielding a fluffy, dried gel. Using an agate mortar, the dried gel was made into a fine powder to ensure uniform particle size and prevent agglomeration.

The calcination process involved two steps. Initially, the fine powder was calcined at 350 °C for 3 hours with a controlled heating and cooling rate of 3 °C/min to eliminate residual organic materials and initiate phase formation. To promote crystallization and phase purity, the calcined product was annealed at 600 °C for 2 hours in a muffle furnace. This thermal treatment produced orange-colored $BiFeO_3$ nanoparticles, confirming the successful synthesis of the desired perovskite structure [17,18].

2.3. *Characterization methods*

To identify chemical bonds in the synthesized powder Fourier Transform Infrared (FTIR) Spectroscopy [Spectrum 100, Perkin Elmer] was performed. X-ray diffraction (XRD) was used for structural characterisation using a Siemens D500 X-ray diffractometer, which was run at 45 kV and 40 mA accelerating voltage. In accordance, the applied current was established. Over the 2θ range of 0–90°, a scan rate of 5° min^{-1} was employed. Scanning Electron Microscopy (SEM) [Hitachi X650, Japan] to analyse the morphology and particle size of the sample. The UV-DRS spectrum was recorded using a Shimadzu Lambda 900 Spectrophotometer over a wavelength range of 240–800 nm.

2.4. *Photocatalytic activity*

An indigenously designed immersion-type photocatalyst reactor was used for all visible light irradiation studies. Encased in a quartz tube (sealed on one side) and submerged in a cylindrical borosilicate reactor (1 L capacity), the visible light source was a 500 W Xe arc lamp (intensity = 137 $mWcm^{-2}$).

The catalyst and dye solution mixture was put into the reactor, and a water bath that was constantly circulating kept the suspension uniform. Using suitable dilutions, dye solutions

with different concentrations were made from a stock solution (100 mg L^{-1}). To reach adsorption-desorption equilibrium between the catalyst and dye solution, the suspensions were magnetically agitated in the dark for 20 min prior to irradiation. The equilibrium concentration of the dye (Ceq) in contact with the catalyst was considered the true dye concentration at the start of irradiation, thus taken as C_0 for photo degradation kinetics.

0.1 N NaOH and 0.1 N HCl were used to adjust the pH of the solution. Throughout the experiment, samples were withdrawn at regular intervals, and the decrease in dye absorbance at λ_{max} = 620 nm (the characteristic wavelength of Malachite green dye) was recorded. After centrifugation, the aliquots were filtered using Whatman filter paper (No. 42) for removing catalyst.

Systronics double-beam UV-Visible spectrophotometer 2203 was used to determine the residual dye concentration in the samples. The absorbance at λ_{max} = 620 nm was converted to residual concentration using pre-determined calibration curves for Malachite Green dye. The formula for the dye degradation % at any time t:

Degradation % = $[(C_0 - C_t) / C_0] \times 100$

where:

- C_0 = Concentration of dye prior to photo irradiation (mg L^{-1})
- C_t = Concentration of dye after photo irradiation (mg L^{-1})

Direct photolysis of the dye was insignificant, as demonstrated by a blank experiment with pure dye (without catalyst) exposed to visible light and continuous stirring for 30 min.

3. Results and Discussion

3.1. *Characterization*

3.1.1. *FTIR spectra*

FTIR spectra of the $BaBiO_3$ powder in 4000 to 500 cm^{-1} range is shown in Fig. 1. Metal oxide formation was primarily attributed to bands between 700 and 400 cm^{-1}. The bands at 450 cm^{-1} and 549.68 cm^{-1} can be attributed to the modes of Fe–O stretching vibrations and Fe–O bending vibration, respectively. This behavior is typical of $[FeO_6]$ octahedra in the perovskites, confirming the nanostructured rhombohedral $BiFeO_3$ perovskite phase [19]. The prominent peak at 845.46 cm^{-1} is ascribed to bending vibrations of Bi-O, suggesting highly crystalline $BiFeO_3$ phase formation [20]. This band at about 1066 cm^{-1} is caused by the Bi-O bond vibrating [21,22]. Strong vibration of residual nitrogen groups (NO_3^- stretching vibration) attribute to the formation of band at 1385 cm^{-1} in $BiFeO_3$ [23]. The band at 1629.28 cm^{-1} correspond to nitrile (C≡N) [24]. Because of the absorption of water molecules from the air, the peaks at 3451.01 cm^{-1} are attributed to the symmetric and antisymmetric stretching of H_2O and OH^- groups.

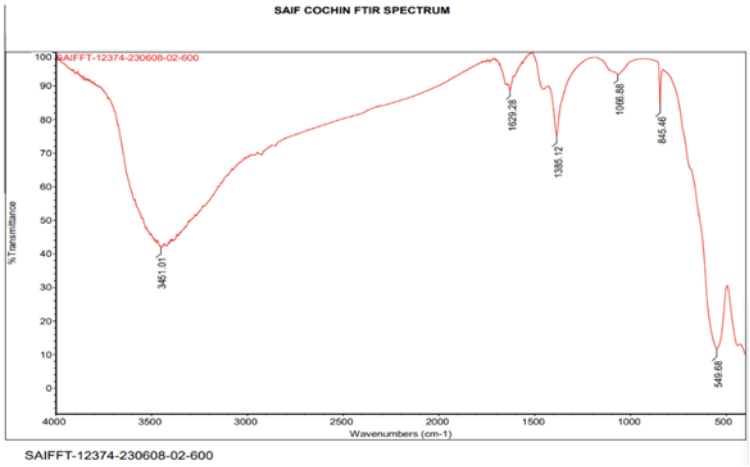

Fig. 1. FTIR spectra of $BiFeO_3$ perovskite prepared at 600 °C.

3.1.2. *XRD patterns*

XRD of samples calcined at 350 °C (a) and 600 °C (b) are displayed in Fig. 2. The XRD pattern at 350 °C indicates the onset of a crystalline perovskite-type structure of $BiFeO_3$, this crystallinity increased with increase in temperature i.e. 600 °C as shown in Fig. 2(b). Fig. 2(b) exhibits fewer impurity peaks than at 350 °C shown in Fig. 2(a), which show additional peaks beyond $BiFeO_3$. Fundamental peaks related to $BiFeO_3$ phase get stronger as the temperature rises, whereas secondary phases get weaker. Previous studies attribute these impurity peaks to $Bi_2Fe_4O_9$ (mullite) and $Bi_{25}FeO_{39}$ (sillenite) [25]. However, non-perovskite phases are well-controlled, confirming the phase purity of synthesized $BiFeO_3$. Bismuth loss was minimized due to the low-temperature synthesis method. Thus, a fully crystalline single-phase $BiFeO_3$ oxide with a distinct perovskite structure was produced at 600 °C, as shown in Fig. 2(b).

Structural characterization matched the XRD pattern with the standard $BiFeO_3$ pattern (JCPDS No. 86-1518), indexing the intensity profile as a hexagonal perovskite phase with a distorted rhombohedral structure (R_3c),
Where a = b = 5.587 Å, c = 13.867 Å, $\alpha = \beta = 90°$, $\gamma = 120°$.

Diffraction peaks for $BiFeO_3$ at $2\theta = 22.31°$, 31°, 32.5°, 39°, 46°, 52°, 57.4° and 67° match the (012), (110), (202), (024), (121), (300), (220) and (221) crystalline planes of the rhombohedral $BiFeO_3$ structure [26]. The perovskite $BiFeO_3$ phase in the rhombohedral R3c space groups visible in Fig. 2(b) is further supported by the clear splitting of peaks (104) and (110). Thus, the successful synthesis of well-crystallized, pure-phase bismuth ferrite is confirmed. The results are consistent with previous studies [26,27]. The average crystallite size (*d*) was calculated from the XRD patterns (Fig. 2b) using the Scherrer formula, $d = k\lambda/\beta\cos\theta$, where k is the dimensionless shape factor with a typical value of about 0.9, λ is the wavelength of Cu Kα radiation with the value of 1.5418 Å, θ is the Bragg angle for the

various diffraction peak and β is the full width at half maximum (FWHM) intensity of the corresponding diffraction peak [28,29].
Scherrer's equation is:

$$D = (k\lambda)/(\beta \cos\theta)$$

The average crystallite size was found to be 30.06 nm, using Scherrer's formula as evident from Table 1.

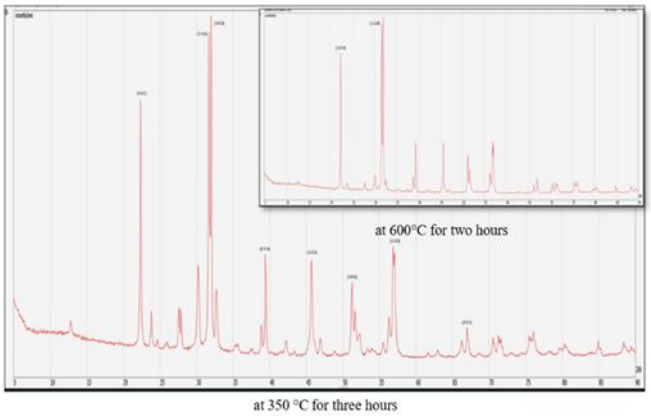

Fig. 2. XRD pattern of $BiFeO_3$ calcined (a) at 350 °C for three hour and (b) at 600 °C for two hours.

Table 1. Crystallite size for various diffraction peaks for $BiFeO_3$ when annealed at 600 °C.

Diffraction peak	2 θ (degree)	D (Å)	Width at half maximum (FWHM)	FWHM (in radians)	Size (nm)	Average (nm)
1	22.3281	3.9788	0.1713	0.002990	47.25	
2	31.830	3.113	0.5637	0.009765	14.66	
3	39.4083	2.2850	0.1833	0.003199	46.03	30.06
4	45.6895	1.9842	0.2515	0.004390	34.27	
5	51.343	1.7781	0.5846	0.010204	15.08	
6.	56.9669	1.6152	0.3918	0.006818	23.07	

EDX spectroscopy analysis of $BiFeO_3$ nanoparticles (Fig. 4) also confirmed high purity, indicating the existence of Bi, Fe, and O elements, validating XRD results [30].

3.1.3. *SEM images*

Fig. 3 shows the SEM micrographs of $BiFeO_3$ powder prepared at 600 °C at different magnifications. Agglomerated morphology and granular particle shapes are evident in the FESEM micrographs of $BiFeO_3$ samples. Particle sizes were calculated using ImageJ Software from micrographs at different magnifications (1000x to 3500x), showing crystal sizes in the range of 150 nm – 440 nm with varying polygonal morphology (e.g., spheroid, ellipsoid, and some hexagonal shapes) which are consistent with earlier reports [31].

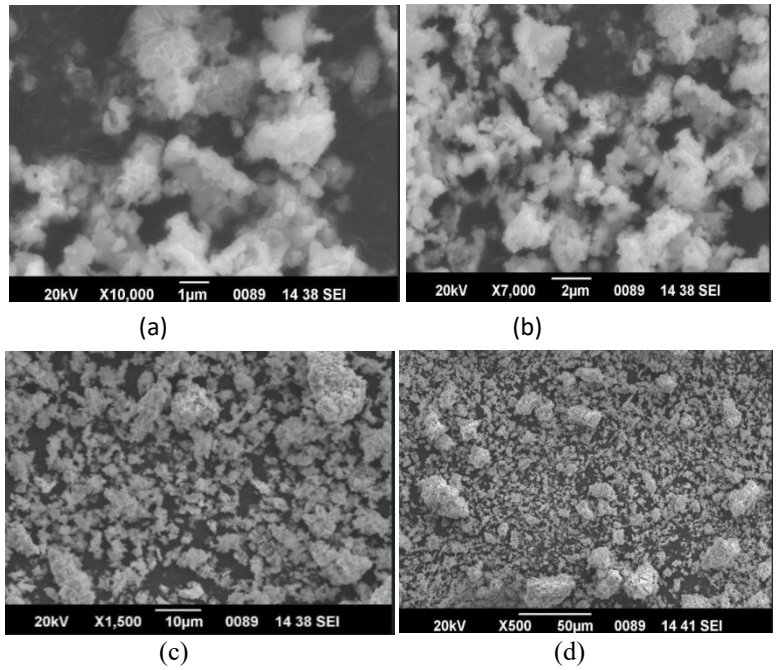

Fig. 3. SEM micrograph of $BiFeO_3$ nanoparticles (a) 1000x (b) 7000x (c) 1500x (d) 3500x magnifications.

The variation in particle sizes suggests the presence of agglomerates. Primary particles frequently form agglomerates with a low surface-to-volume ratio in the Pechini method in order to reduce surface energy [32]. Aggregation of smaller particles (in the nm range) may result in larger particles on the surface. It is worth mentioning here that the average crystallite size (30.06 nm), calculated from the XRD patterns using the Scherrer formula, was smaller than the particle size from FESEM micrographs because a particle comprises several crystallites and they measure different material aspects [33,34]. Agglomeration is caused by the reduced volume-to-surface-area ratio of nanoparticles [35]. The results align with earlier reports [36].

3.1.4. *EDX spectra*

The EDX spectrum, which is displayed in Fig. 4, demonstrated chemical homogeneity by confirming that the $BiFeO_3$ perovskite nanostructure's stoichiometry ratio and chemical composition match the nominal composition (1:1:3). The presence of Bi, Fe, and O components was clearly evident. The theoretical atomic percentages for Bi, Fe, and O in $BiFeO_3$ are 20 %, 20 %, and 60 %, respectively. Observed values revealed atomic percentages of bismuth, iron, and oxygen (Table 1) as 19.65 %, 17.6 %, and 62.75 %, respectively, closely aligning with theoretical values and verifying high nanoparticle purity.

The Bi/Fe ratio of 1.066 is near the stoichiometric ratio for a pure $BiFeO_3$ phase, consistent with earlier reports [37].

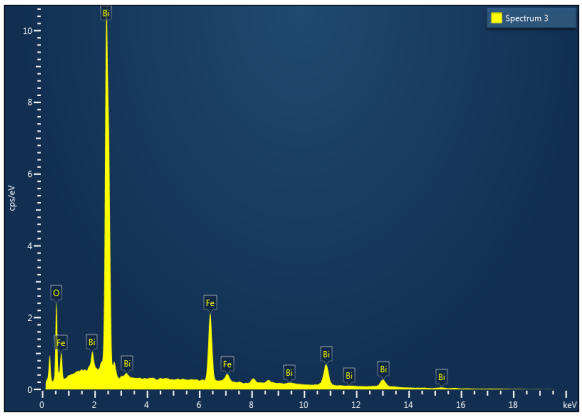

Fig. 4. EDX analysis of $BiFeO_3$ nanoparticles annealed at 600 °C.

Table 2. EDX weight and atomic ratios of pure $BiFeO_3$ nanoparticles annealed at 600 °C.

Element	Line Type	Weight %	Atomic %
O	K series	16.48	62.75
Fe	K series	16.13	17.6
Bi	M series	67.39	19.65
Total		100	100

3.1.5. *UV – DRS*

The optical characteristics of as-prepared $BiFeO_3$ were studied using UV-Visible spectra recorded over 300–800 nm, as shown in Fig. 5. The diffuse reflectance spectra of $BiFeO_3$ (Fig. 5a) exhibited a strong fundamental absorption edge at 550 nm, indicating potential as a visible-light-driven photocatalyst. Tauc's formula was used to calculate the optical band gap (E_g) [38]. In powder sample analysis, the Kubelka–Munk (K–M) function is frequently utilized to convert diffuse reflectance into equivalent absorption coefficients, as seen in Equation.

$\alpha = F(R) = (1 - R^2/(2R)$

where $F(R)$ is the K–M function and R = reflectance. The modified Tauc relation is applied to calculate the optical energy band gap:

$\alpha h\nu = A(h\nu - E_g)^n$

where α = absorption coefficient, h = Planck's constant, A = constant, E_g is the optical energy band gap, and for direct transitions $n = 1/2$.

The linear part of the $(\alpha h\nu)^2$ [Kubelka-Munk Function] vs $h\nu$ plot was extrapolated to $(\alpha h\nu)^2 = 0$ in order to determine the E_g values.

Fig. 5(b) demonstrates the Kubelka-Munk conversion spectrum [39]. Extrapolation of the linear curves to zero absorption yielded E_g for direct transition. The E_g value of $BiFeO_3$

from above Fig. 5(b) is found to be 1.9 eV which is significantly lower than the observed values for the synthesized $BiFeO_3$ in the range 2.25 - 2.8 eV reported from previous research work [40].

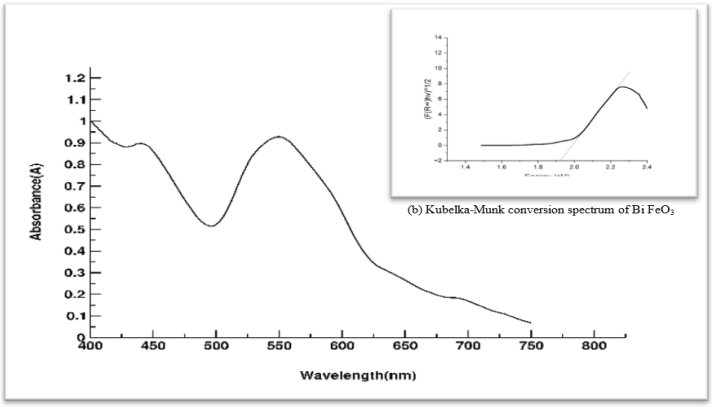

Fig. 5(a). UV-vis Absorbance spectra of $BiFeO_3$.

Fig. 5. UV-vis Absorbance spectra of $BiFeO_3$ prepared at 600 °C (a) the inset diagram and (b) shows an estimation of band gap energy by extrapolation method.

3.2. *Photodegradation studies*

With a constant photocatalyst loading of 0.75 g L^{-1}, the initial dye concentration can be varied from 20 mg L^{-1} to 80 mg L^{-1} to determine the effect of the initial concentration on the rate of degradation. As the dye concentration rises to 40 mg L^{-1}, the degradation efficiency increases after which it drops, as shown in Fig. 6. This pattern is probably caused by a greater mass transfer driving force as a result of more molecules vying for the binding sites on $BiFeO_3$ that are accessible for adsorption as the initial dye concentration rises.

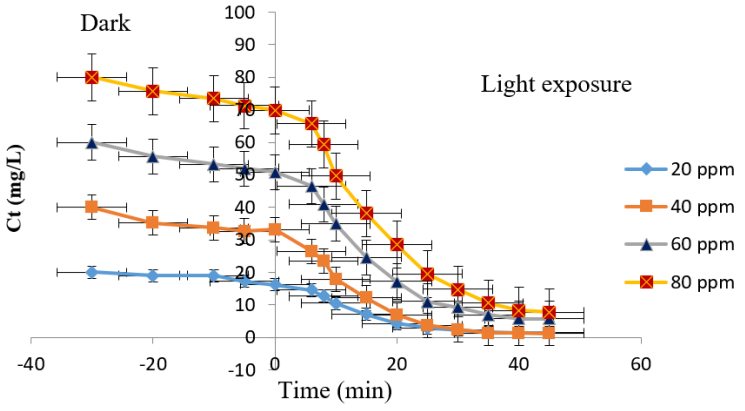

Fig. 6. Variation of dye concentration versus time for different Malachite green initial concentration. (Experimental condition: Bi FeO_3= 0.75 g L^{-1}, pH=6.0, and Temp. = 308 K).

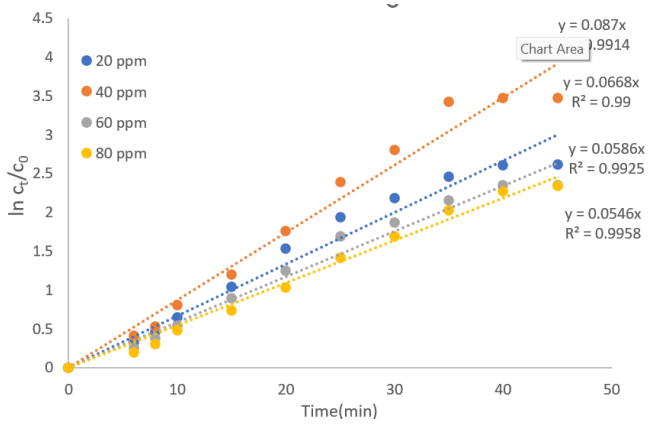

Fig. 7. Linear variation of ln C_t/C_o versus time for the photocatalytic degradation of Malachite green dye at different initial concentration. (Experimental condition: [Bi FeO_3] = 0.75 g L^{-1}, pH = 6.0, and Temp. = 308 K).

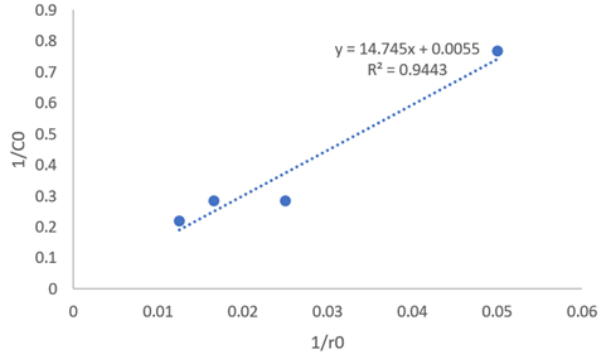

Fig. 8. Langmuir-Hinshelwood plot for visible light photodegradation of Malachite green dye by $BiFeO_3$ photocatalyst.

The saturation of binding sites results in a decrease in adsorption above the optimal concentration. Furthermore, at greater dye concentrations, the dye absorbs more light than the photocatalyst does. As a result, the dye creates an inner filter effect at high starting concentrations, meaning it begins to filter incident light [41].

From a mechanistic and application standpoint, it is crucial to investigate how the amount of $BiFeO_3$ affects the photocatalytic reaction rate in dye degradation. Thus, the effect of photocatalyst dose on the photodegradation rate of the Malachite green dye was examined by changing the catalyst dose from 0.5 g L^{-1} to 1.0 g L^{-1} at an initial dye concentration of 40 mg L^{-1}. Fig. 7 makes it evident that dye degradation occurs more quickly at a catalyst dose of 0.75 g L^{-1} as opposed to 0.5 or 1.0 g L^{-1}. The increased total surface area and availability of the photocatalyst's active sites due to the higher catalyst loading are responsible for the augmentation in the degradation rate, which is further

increased. After exceeding the ideal catalyst loading, the opacity caused by extra catalyst lowers light penetration and enhances the scattering effect, which lowers the degradation rate. These findings align with previous research [42].

The equation $r = r_1 + r_2$ expresses the total photocatalytic degradation rate, where r, r_1, and r_2 stand for the net degradation, photolysis rate, and photocatalysis rate, respectively. In blank studies, no dye degradation was seen. indicating that visible light alone plays a negligible effect. Therefore, it may be said that visible light and catalyst loading work together to cause the dye concentration to decrease [43]. In the breakdown process of heterogeneous photocatalysts, the first step of the reaction is believed to be the adsorption of dye on the catalyst surface [44]. Accordingly, Malachite green adsorption on the $BiFeO_3$ surface is depicted in Fig. 6 as a function of time. The outcome shows that there is a 15 % drop in Malachite green concentration. The concentration of the dye after the 15 minutes dark adsorption is taken as the initial concentration (C_o). The following equation can be used to describe the pseudo-first-order kinetic rule that governs the photocatalytic degradation of Malachite green across the $BiFeO_3$ surface.

$$L_n\, C_o/C_t = Kapp * t$$

After recording and fitting the curves of $– L_n\, C_o/C_t$ against 't' linearly, the slope of the straight line is used to determine the value of the pseudo-first order rate constant (Kapp) (Fig. 7). The initial reaction rate (R_o) is calculated by multiplying the computed Kapp by the corresponding initial dye concentration. Many research studies indicate that the Langmuir-Hinshelwood (LH) model is used to characterize the photocatalytic degradation kinetics [45].

The following expressions provide the LH model's linear form:

$$1/R_o = 1/k_r + 1/k_r \cdot K_{LH} \cdot C_o$$

Here, the adsorption constant (Langmuir-Hinshelwood constant) is denoted by K_{LH}, and the reaction rate constant by k_r. The graph between r_o^{-1} and C_o^{-1} is displayed in Fig. 8 as a straight line with an intercept of Kr^{-1} and a slope of $(kr.K_{LH})^{-1}$. K_r and K_{LH} have respective values of 14.745 mg $L^{-1}min^{-1}$ and 0.0055 L mg^{-1}.

4. Conclusion

In this study, the Pechini method was used to synthesize pure $BiFeO_3$ nanoparticles at 600 °C as an efficient photocatalyst with citric acid acting as a chelating agent. The metal-oxide bands at 450 cm^{-1} and 549.68 cm^{-1} in the observed FTIR verify that $BiFeO_3$ has crystallized in a perovskite structure. XRD results indicated the formation of pure-phase $BiFeO_3$ crystallized into a rhombohedral structure, with a crystallite size of 30.06 nm determined by Scherer's formula. The SEM image of the calcined powder shows nano particles in the range of 150 nm – 440 nm. $BiFeO_3$ nanoparticles delivered an optical bandgap of 1.9 eV from the diffuse reflectance spectrum with broad absorbance around 550 nm, unveiling an exceptional photocatalytic activity under visible light illumination. At a photocatalyst dose of 0.75 g L^{-1}, an initial concentration of 40 mg L^{-1} Malachite green dye at a natural pH (5.5) and temperature of 35 °C the best degradation results are achieved. The photodegradation

kinetics of the dye follows a pseudo-first-order Langmuir-Hinshelwood model. Finally, it is concluded that the Pechini method's low-temperature synthesis of $BiFeO_3$ may unquestionably be used as a photocatalyst for the degradation of wastewater containing dyes.

Acknowledgment

The authors are thankful to DST FIST Laboratory Department of Chemistry, Government College, Kota for providing necessary facilities during the Research work.

References

1. West and Phillip, Castlemaine Nat. **31**, 3 (2006). https://doi.org/10.5962/p.401080
2. J. W. Lee, S. P. Choi, R. Thiruvenkatachari, W. G. Shim, and H. Moon, Water Res. **40**, 435 (2006). https://doi.org/10.1016/j.watres.2005.11.034
3. S. D. Gosling, S. Vazire, S. Srivastava, and O. P. John, Am. Psychol. **59**, 93 (2006). https://doi.org/10.1037/0003-066X.59.2.93
4. K. Polat and M. Yurdakoc, J. Turk. Chem. Soc. A: Chem. **6**, 261 (2019). https://doi.org/10.18596/jotcsa.526822
5. S. Suzuki, A. Iwase, and A. Kudo, Catal. Sci. Technol. **10**, 4912 (2020). https://doi.org/10.1039/D0CY00600A
6. Q. Liu, Y. Chai, Zhang, J. Ren, and W. L Dai, Appl. Catal. B: Environ. **205**, 505 (2017). https://doi.org/10.1016/j.apcatb.2016.12.065
7. S. Alkaykh, A. Mbare, and E. E. Ali-Shattle, Heliyon **6**, ID e03663 (2020). https://doi.org/10.1016/j.heliyon.2020.e03663
8. T. Xian, X. Ma, X. Sun, C. Sun, H. Wang, L. Di, K. Ma, and H. Yang, Opt. Mater. **149**, ID 115054 (2024). https://doi.org/10.1016/j.optmat.2024.115054
9. T. Zhou, T.Zhai, H. Shen, J. Wang, R. Min, K. Ma, and G. Zhang, Chemosphere **339**, ID 139678 (2023). https://doi.org/10.1016/j.chemosphere.2023.139678
10. M. Kumar, K. L. Yadav, and G. D. Varma, Mater. Lett. **62**, 1159 (2008). https://doi.org/10.1016/j.matlet.2007.07.075
11. V. Fruth, M. Popa, J. M. Calderon-Moreno, E. M. Anghel, D. Berger, M. Gartner, and M. Zaharescu, J. Eur. Ceram. Soc. **27**, 4417 (2007). https://doi.org/10.1016/j.jeurceramsoc.2007.02.175
12. C. Chen, J. Cheng, S. Yu, L. Che, and Z. Meng, J. Cryst. Growth **291**, 135 (2006). https://doi.org/10.1016/j.jcrysgro.2006.02.048
13. X. Xu, T. Guoqiang, R. Huijun, and X. Ao, Ceram. Int. **39**, 6223 (2013). https://doi.org/10.1016/j.ceramint.2013.01.042
14. D. S. García-Zaleta, A. M. Torres-Huerta, M. A. Dominguez-Crespo, J. A. Matutes-Aquino, A. M. González, and M. E. Villafuerte-Castrejón, Ceram. Int. **40**, 9225 (2014). https://doi.org/10.1016/j.ceramint.2014.01.143
15. K. V. Kumar, K. Porkodi, and A. Selvaganapathi, Dyes Pigment **75**, 246 (2007). https://doi.org/10.1016/j.dyepig.2006.05.035
16. K. V. Kumar, K. Porkodi, and F. Rocha, A Theoret. Study **9**, 82 (2008). https://doi.org/10.1016/j.catcom.2007.05.019
17. X. Wang, N. Zhang, and G. Wang, In MATEC Web of Conf. **238**, ID 03007 (2018). https://doi.org/10.1051/matecconf/201823803007
18. M. M. Parvez, M. E. Haque, M. Akter and H. Ferdous, Int. J. Sci. Eng. Investig. **101**, 35 (2020).
19. V. A. Reddy, N. P. Pathak, and R. Nath, J. Alloys Compd. **543**, 206 (2012). https://doi.org/10.1016/j.jallcom.2012.07.098

20. H. Yang, T. Xian, Z. Q. Wei, J. F. Dai, J. L. Jiang, and W. J. Feng, J. Sol-Gel Sci. Technol. **58**, 238 (2011). https://doi.org/10.1007/s10971-010-2383-6
21. M. Čebela, B. Janković, R. Hercigonja, M. J. Lukić, Z. Dohčević-Mitrović, D. Milivojević, and B. Matović, Process. Appl. Ceram. **10**, 201 (2016). https://doi.org/10.2298/PAC1604201C
22. I. O. Troyanchuk, A. N. Chobot, O. Mantytskaya, and N.V. Tereshko, Inorg. Mater. **46**, 424 (2010). https://doi.org/10.1134/S0020168510040187
23. B. J. Rani, G. Ravi, R. Yuvakkumar, and M. Thambidurai, J. Sol-Gel Sci. Technol. **91**, 247 (2019). https://doi.org/10.1134/S0020168510040187
24. M. A. Almessiere, S. Güner, Y. Slimani, A. Baykal, S. E. Shirsath, A. D. Korkmaz, R. Badar and A. Manikandan, J. Mol. Struct. **1248**, ID 131412 (2022). https://doi.org/10.1016/j.molstruc.2021.131412
25. A. Sagdeo, P. Mondal, A. Upadhyay, A. K. Sinha, A. K. Srivastava, S. M. Gupta, and S. K. Deb, Solid State Sci. **18**, 1 (2013). https://doi.org/10.1016/j.solidstatesciences.2012.12.017
26. B. Kumari, P. R. Mandal, and T. K. Nath, Adv. Mater. Lett. **5**, 84 (2014). https://doi.org/10.5185/amlett.2013.fdm.36
27. N. Zhang, D. Chen, F. Niu, S. Wang, L. Qin, and Y. Huang, Sci. Rep. **6**, ID 26467 (2016). https://doi.org/10.1038/srep26467
28. J. A. Bhalodia, P. V. Kanjariya, S. R. Mankadia, and G. D. Jadav, Int. J. Chem. Tech. **6**, 2144 (2014).
29. J. S. Bergstrom, Mechanics of Solid Polymers: Theory and Computational Modeling (Elsevier, Netherland, 2015). https://doi.org/10.1016/C2013-0-15493-1
30. E. A. V. Ferri, E. A. V. Santos, E. Radovanovic, R. Bonzanini, and E. M. Girotto, J. Braz. Chem. Soc. **19**, 1153 (2008). https://doi.org/10.1590/S0103-50532008000600015
31. V. B. Sherkar and A.V. Mancharkar, Int. Res. J. Sci. Eng. Special Issue **A2**, 10 (2018).
32. D. Tiwari and S. Dunn, J. Mater. Sci. **44**, 5063 (2009). https://doi.org/10.1007/s10853-009-3472-1
33. M. M. Ibrahim, E. M. M. Ibrahim, S. A. Saleh, and A. A. Hakeem, J. Alloys Compd. **429**, 19 (2007). https://doi.org/10.1016/j.jallcom.2006.03.085
34. J. S. Bangruwa, B. K. Vashisth, N. Singh, and V. Verma, J. Alloys Compd. **739**, 319 (2018). https://doi.org/10.1016/j.jallcom.2017.12.281
35. S. Gupta, M.Tomar, A. R. James and V. Gupta, J. Mater. Sci. **49**, 5355 (2014). https://doi.org/10.1007/s10853-014-8243-y
36. N. R. Niloy, M. I. Chowdhury, S. Anowar, J. Islam, and M. M. Rhaman, J. Nano- Electron. Phys. **12**, ID 05015 (2020). https://doi.org/10.21272/jnep.12(5).05015
37. H. Sangian, O. Mirzaee, and M. Tajally, Adv. Ceram. Prog. **3**, 31 (2017).
38. M. Sertkol, S. Güner, M. A. Almessiere, Y. Slimani, A. Baykal, H. Gungunes, and A. Manikandan, Mater. Chem. Phys. **284**, ID 126071 (2022). https://doi.org/10.1016/j.matchemphys.2022.126071
39. M. Sukumar, M. Mathankumar, C. S. Dash, M. Sundararajan, M. Ubaidullah, S. F. Shaikh, and J. Dhanraj, Res. Square **1** (2022). https://doi.org/10.21203/rs.3.rs-1250457/v1
40. G. Catalan and J. F. Scott, Adv. Mater. **21**, 2463 (2009). https://doi.org/10.1002/adma.200802849
41. Y. Fan, N. W. Duncan, M. De Greck, and G. Northoff, Neurosci. Biobehav. Rev. **35**, 903 (2011). https://doi.org/10.1016/j.neubiorev.2010.10.009
42. M. R. Sohrabi, N. Mansouriieh, M. Khosravi, and M. Zolghadr, Water Sci. Technol. **71**, 1367 (2015). https://doi.org/10.2166/wst.2015.106
43. N. Mansouriieh, M. Reza Sohrabi, R. Pouramir Vajargah and H. Roudbaraki, Water Sci. Technol. **76**, 1992 (2017). https://doi.org/10.2166/wst.2017.339
44. X. Yin, F. Xin, F. Zhang, S. Wang, and G. Zhang, Environ. Eng. Sci. **23**, ID 1000 (2006). https://doi.org/10.1089/ees.2006.23.1000
45. J. F. Effiong, A. E. Nyong, and C. U. G. Obadimu, J. Mater. Environ. Sci. **14**, 935 (2023). https://doi.org/10.9734/ajacr/2023/v13i2240